Zeolite/Polymer Composites Prepared by Photopolymerization: Effect of Compensation Cations on Opacity and Gas Adsorption Applications

Yuanyuan Gao, Yagmur Deniz Karatas, Habiba Nouali, Jean-Pierre Salomon, Jacques Lalevée, Angelique Simon-Masseron

Zeolite/Polymer Composites Prepared by Photopolymerization: Effect of Compensation Cations on Opacity and Gas Adsorption Applications

Yuanyuan Gao[1,2], Yagmur Deniz Karatas[1,2], Habiba Nouali[1,2], Jean-Pierre Salomon[3,4,5], Jacques Lalevée[1,2*], Angélique Simon-Masseron[1,2*]

[1] Université de Haute-Alsace, CNRS, IS2M UMR 7361, 68100 Mulhouse, France

[2] Université de Strasbourg, 67081 Strasbourg, France

[3] Université de Bourgogne Franche-Comté, Laboratoire de Nanomédecine, Imagerie, Thérapeutique EA4662, 25030 Besançon, France

[4] Visiting Professor. "Dental Materials and Prosthodontics Department" and "Optical Properties Division" in Post Graduate Program in Dentistry"; Araraquara's Dental School, UNSEP, São Paulo, Brésil

[5] Clinical Associate Professor. "Department of Restorative Dentistry" at Oregon Health and Science University, Portland, Oregon, USA.

***Corresponding authors:**

Angélique Simon-Masseron, angelique.simon-masseron@uha.fr

Jacques Lalevée, jacques.lalevee@uha.fr

Abstract

The fabrication of structured zeolite adsorbents through photopolymerization-based 3D printing which offers a solution to the limitations of conventional shaping techniques has been demonstrated but many parameters still need to be optimized. In this study, we studied the influence of zeolite compensation cations on the photopolymerization and the composite's properties. Modified zeolites (LTA 4A and FAU 13X exchanged with K^+, Li^+, Sr^{2+}, Ca^{2+} or Mg^{2+}) were incorporated in PEGDA with BDMK as photoinitiator, and the formulation was cured under mild conditions (LED@405 nm, room temperature, under air). Our results indicate that the nature of zeolite compensation cations affects the colorimetric properties of polymer/zeolite composites: a better translucency parameter results in higher depth of cure. After calcination at 650 °C and complete removal of PEGDA, pure zeolitic monoliths were tested for adsorption of gas molecules of interest (carbon dioxide, dichlorobenzene and water). Structured 4A and 13X monoliths obtained by 3D printing exhibit comparable adsorption capacity to commercial beads prepared from the same zeolites. This study enhances our understanding of the photopolymerization process involved in the production of polymer/zeolite composites. These composites are used in the fabrication of zeolitic objects through 3D printing, offering potential solutions to various environmental and dental challenges.

Keywords

Polymer/zeolite composite, photopolymerization, 3D printing, ion-exchange, adsorption

Introduction

In the last decades, zeolites have been extensively studied for their ability of gas adsorption due to their unique porous structure and high surface area. The adsorption of carbon dioxide (CO_2) has received significant attention due to the pressing need to mitigate climate change and reduce greenhouse gas

emissions. As a class of crystallized microporous (pore size < 2 nm) aluminosilicates, zeolites have also been utilized for the adsorption of other gases, such as methane (CH_4), nitrogen oxides (NO_x), and volatile organic compounds (VOCs).[1,2] The gas adsorption capacity of zeolites is influenced by various factors such as the structural type, the pore size and the chemical composition of the zeolite, as well as the chemical properties of the adsorbates. The general chemical formula of zeolite is $M_{2/n}O.Al_2O_3.xSiO_2.yH_2O$, where 'x' is equal to or greater than 2 and 'n' is the valence of the extra-framework cation 'M', or so-called compensation cation.[3] The Si/Al molar ratio varies between 1 in LTA, to infinite in silicalite-1, switching the structure from highly hydrophilic to hydrophobic.[4] The compensation cations also have an effect on the zeolite's properties. For example, LTA 3A (KA, zeolite A exchanged with K^+) is commonly used in the ethanol drying processes[5] while LTA 5A (CaA, zeolite A exchanged with Ca^{2+}) selectively adsorbs linear alkanes from a mixture of branched alkanes.[6] LiA was proposed to be used in drug delivery while LiX (FAU 13X exchanged with Li^+)[7] was reported to be effective to separate nitrogen from air.[8] Zinc (Zn^{2+}), silver (Ag^+) and copper (Cu^{2+}) exchanged zeolites were reported to have antibacterial properties.[9]

In the LTA structure type, the α-cage (or so-called supercage) with a diameter of 1.14 nm is surrounded by eight sodalite cages (β-cages) (Figure 1). The access to this supercage is through apertures (8-membered rings windows) the diameter of which varies according to the number and the nature of the compensation cations, with a minimum diameter of 0.44 nm.[10] Such cations are located in specific place as reported in Figure 1a for LTA: (i) site I, at the center of a six-membered ring constituting one of the eight β-cages; (ii) site II, near the 8-membered ring thus directly blocking the entrance to the supercage; (iii) site III, inside the cavity that close to the four-membered ring.[10,11] As for FAU structure type, 10 sodalite cages are linked through hexagonal prisms to form a supercage (α-cage , 1.3 nm diameter), accessed through 12-membered rings windows with a diameter of about 0.74 nm. Locations of compensation cations are identified in Figure 1b: (i) site I, in the hexagonal prism, either in its center or shifted from it; (ii) site I', in the sodalite cage toward the hexagonal prism close to the 6-membered ring window; (iii) site II, at the center of the 6-membered ring window between the sodalite cage and the

supercage; (iv) site II', in the sodalite cage close to the 6-membered ring window; (v) sites III and III', in the supercage close to its 12-membered ring.[10,12]

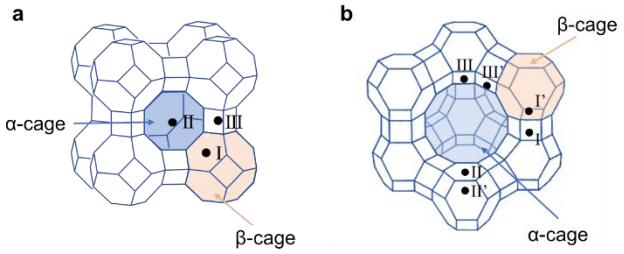

Figure 1. Location of compensation cations in different zeolite structure types: (a) LTA and (b) FAU.

Zeolite is obtained in powder forms after synthesis and therefore, must be shaped for industrial usage.[13] However, the traditional zeolite shaping approaches can only produce simple forms like beads, pellets or extrudates. Furthermore, the disadvantages of using binders, such as reduced porosity and thermal stability, can severely limit the effectiveness of zeolites.[14,15] As a result, 3D printing processes have been extensively studied in recent years as a versatile technique to fabricate zeolitic objects with varying sizes, shapes, and complexities.[16] The most commonly used approach is to mix zeolite with a binder, as well as a small amount of plasticizer or other additives to achieve an appropriate level of fluidity.[17–23] After stirring, the mixture is extruded to create a self-standing support structure. For instance, Thakkar et al. reported the fabrication of 5A and 13X monoliths *via* direct ink write (DIW) using bentonite as the permanent binder for CO_2 adsorption.[18] In another work, Li and coworkers prepared 3D printed HZSM-5 and HY monoliths by DIW for catalytic cracking of n-hexane.[23]

Among various 3D printing techniques, photopolymerization has attracted attention for its unique advantages such as high production rate, mild reaction temperature, low level of volatile organic compounds (VOCs), low energy consumption, excellent spatial and temporal control, etc. It is widely applied in the domains of dental materials,[24] coatings,[25] and adhesives.[26] The photopolymerization process can be carried out using a variety of light sources, including lasers, DLP (digital light processing) projectors, or LCD (liquid crystal display) screens.[27] These light sources cure the resin by either

selectively exposing it to light, or by projecting an image of the 3D model onto the resin layer. Several works have been done by our team using visible LED light (Light-Emitting Diode) to fabricate structured zeolite adsorbents for adsorption[28–30] and ion-exchange[31] applications. However, adding fillers to the photopolymerizable resin will cause light penetration issues since the filler particles can reflect, absorb, or scatter the light.[32,33] The optical properties of filled system determine not only their aesthetic appearance but also their curing depth and polymerization kinetics.[34] Nevertheless, few studies have been conducted in which the influence of zeolites' properties on photopolymerization is examined.

In this work, the fabrication of structured zeolite composites and monoliths *via* photopolymerization for gas adsorption applications from cation-exchanged FAU 13X and LTA 4A zeolites is described. PEGDA was selected as monomer in this work due to its high polymerization conversion, good compatibility with zeolite and improved light transmittance for the composite.[30] The effects of cations on the photopolymerization, the adsorption and optical properties (particularly the colorimetric properties) are studied.

Results and discussion

Exchanged zeolites

The physico-chemical characterizations of the parent and exchanged zeolites are summarized in Table 1. The exchange rates defined by equation (1) vary from 59% to 99%, depending on the nature of the cation. It is of 0% for parent zeolites with contains only Na^+ cations.

Exchanged cations are well dispersed into LTA or FAU zeolites according to EDX analyses (Figure S2). Li^+ shows lower selectivity than other alkali cations[35] and the relatively low magnesium ion exchange rate can be explained by the steric effect of the large hydration spheres around Mg^{2+} ions, which makes it difficult to enter the sodalite cages of LTA and FAU zeolites.[36] The charge compensating rate defined as the molar ratio between compensation cations with χ charge and aluminum (Na + χ Me)/Al is always close to 1 indicating that no extra framework aluminum species are formed during the exchange

process.

	Si/Al	Charge compensating rate[a]	Exchange rate[b]	chemical formula[c]	Water content (%)	S_{BET} (m^2/g)	S_{ext} (m^2/g)	V_{micro} (cm^3/g)
NaA	0.96	1.10	0%	$Na_{12}[Si_{12}Al_{12}O_{48}]\cdot 26H_2O$	21.3	-	-	-
LiA	0.95	-	59%	$Na_{4.9}Li_{7.1}[Si_{12}Al_{12}O_{48}]\cdot 22H_2O$	19.8	-	-	-
KA	0.96	1.02	72%	$Na_{3.4}K_{8.6}[Si_{12}Al_{12}O_{48}]\cdot 21H_2O$	17.3	-	-	-
SrA	0.97	1.04	85%	$Na_{1.8}Sr_{10.2}[Si_{12}Al_{12}O_{48}]\cdot 33H_2O$	20.3	611	0.8	0.22
CaA	0.97	1.08	83%	$Na_2Ca_{10}[Si_{12}Al_{12}O_{48}]\cdot 28H_2O$	21.0	720	0.2	0.26
MgA	0.96	1.08	60%	$Na_{4.8}Mg_{7.2}[Si_{12}Al_{12}O_{48}]\cdot 33H_2O$	25.6	672	12.1	0.25
NaX	1.20	1.03	0%	$Na_{87}[Si_{105}Al_{87}O_{384}]\cdot 223H_2O$	23.0	815	12.0	0.30
LiX	1.21	-	63%	$Na_{32.2}Li_{54.8}[Si_{105}Al_{87}O_{384}]\cdot 239H_2O$	25.5	902	10.8	0.34
KX	1.19	0.97	79%	$Na_{18.3}K_{68.7}[Si_{105}Al_{87}O_{384}]\cdot 238H_2O$	21.5	760	7.6	0.28
SrX	1.21	0.99	99%	$Na_{0.9}Sr_{86.1}[Si_{105}Al_{87}O_{384}]\cdot 331H_2O$	23.9	836	9.6	0.31
CaX	1.21	0.98	97%	$Na_{2.6}Ca_{84.4}[Si_{105}Al_{87}O_{384}]\cdot 292H_2O$	26.1	869	26.1	0.32
MgX	1.19	1.00	68%	$Na_{27.8}Mg_{59.2}[Si_{105}Al_{87}O_{384}]\cdot 279H_2O$	27.1	857	18.6	0.32

Table 1. Characteristics of the parent and exchanged LTA and FAU-type zeolites.

[a] Results based on XRF analyses. Me = K^+, Sr^{2+}, Ca^{2+} or Mg^{2+} and χ = 0 for Na^+, 1 for K^+ and 2 for divalent cations. Li^+ cannot be detected by XRF.

[b] Exchange rate is determined by the following equation (based on XRF analyses):

$$\text{Exchange rate (\%)} = \frac{\frac{n_{Na}}{n_{Al}}(BE) - \frac{n_{Na}}{n_{Al}}(AE)}{\frac{n_{Na}}{n_{Al}}(BE)} \times 100 \qquad \text{Equation (1)}$$

where $\frac{n_{Na}}{n_{Al}}(BE)$ is the amount of Na normalized to the amount of Al before exchange and $\frac{n_{Na}}{n_{Al}}(AE)$, the amount of Na normalized to the amount of Al after exchange.

[c] Calculated from TG and XRF analyses.

The X-ray diffraction patterns of the parent zeolites (NaA and NaX) as well as those of their exchanged forms are reported in Figure S3. All exchanged zeolites preserve the structure of their parent materials, which are associated to LTA and FAU structure types. Depending on the nature of the compensation cation, the intensities or positions of some peaks are slightly modified. For example, the (2,2,0) reflection decreases for KA, CaA and SrA but increases in the case of LiA and MgA, in agreement with the results reported in other studies.[37,38] The intensities of (2,2,0) and (3,1,1) peaks have significant variation for FAU zeolite with different compensation cations. Furthermore, for zeolites exchanged with monovalent cations (alkali cations: Li^+, Na^+, K^+), the peaks shift to the left (towards small angles) with the increase of cation radius. The calculated lattice parameters reported in Table 2 confirm the expansion (Na^+ exchanged by K^+) or the contraction (Na^+ exchanged by Li^+) of the unit cell. Such behavior is not observed with divalent cations, whatever the zeolite structure.

Table 2. Lattice parameters for ion-exchanged LTA and FAU zeolites. Both zeolites have cubic unit cell.

Sample	a=b=c (Å)	Cell volume ($Å^3$)	Sample	a=b=c (Å)	Cell volume ($Å^3$)
NaA	12.2993(4)	1860.54(10)	NaX	24.9538(18)	15538.6(19)
LiA	12.0637(4)	1759.65(10)	LiX	24.8122(17)	15275.6(18)
KA	12.3107(4)	1865.74(9)	KX	25.0310(21)	15683.2(23)
CaA	12.2763(10)	1850.2(3)	CaX	24.9148(17)	15465.8(18)
MgA	12.2748(10)	1849.5(3)	MgX	24.9316(3)	15497.1(4)
SrA	12.2967(5)	1859.37(13)	SrX	25.087(3)	15788.3(31)

The space groups for LTA and FAU are Pm-3m and Fd-3m respectively.[39]

Textural properties of zeolite are determined by nitrogen adsorption. From high adsorption at low relative pressure ($p/p° < 0.1$), isotherms (Figure S4) are type I characteristic of microporous solids.[40] No adsorption isotherm was recorded for NaA, LiA and KA, because the monovalent cations are located in or near the 8-membered-ring windows of LTA zeolite (site II), reducing the effective pore aperture (< 0.31 nm). As a result, nitrogen's diffusion was hindered (kinetic diameter of N_2 = 0.315 nm).[41] Similar

observations were reported by Rakoczy et al. for exchanged microcrystalline LTA.[36] SrA presents smaller specific surface areas (611 m^2 g^{-1}) than that of MgA (670 m^2 g^{-1}) and CaA (720 m^2 g^{-1}) due to higher cation radius of Sr^{2+}. The presence of a hysteresis loop in the relative pressure range of ca. 0.45-1.0 (isotherm type IV) for MgA highlights the presence of mesopores. This might be induced by the modification of the crystal morphology (surface covered with nanoparticles and/or outgrowth) shown in Figure S5. It can be observed from these SEM images, the exchanged zeolites retain the size and form of their parent materials except for MgA, which was observed with surface roughness. The specific surface area of exchanged FAU zeolites calculated from isotherms (types I and IV) ranges from 760 to 902 m^2 g^{-1}, and the microporous volumes are close to 0.3 cm^3 g^{-1} (Table 1). For FAU exchanged with monovalent cation, S_{BET} reduces when cation radius increases ($r_{Li+} < r_{Na+} < r_{K+}$) although exchange rates are different.

TG analyses and their derivatives (DTG) as illustrated in Figure S6 showed the substitution of different cations in LTA and FAU can induce different water-uptake capacity. Therefore, the nature of cations affects the affinity between zeolites and water molecules. A continuous weight loss was observed from room temperature to about 400 °C, indicating the desorption of physisorbed water in zeolites. Among the exchanged zeolites, MgA and MgX are the most hydrophilic whereas KA and KX are the most hydrophobic. The position and content of water molecules can further influence the refractive indices of zeolites and the optical properties of polymer/zeolite composites.[42,43]

Polymer/zeolite composites

Figure 2 reports the conversion during the polymerization vs irradiation time. All filled resins were loaded and analysed in a mold with a thickness of 2 mm. The results indicate that pure PEGDA exhibits high reactivity with BDMK, as polymerization initiates rapidly upon exposure to light (t = 10 s) and the conversion of C=C double bond approaches to 100% even at greater depth. The introduction of zeolites causes signal fluctuations because the infrared light is scattered by filler particles. The polymerization yields slightly reduce compared to pure PEGDA due to the light attenuation in filled resin and this phenomenon is more pronounced in the case of FAU zeolites. However, it appears the nature of different

cations has no impact on photopolymerization, indicating that there is no interaction between the photoinitiator BDMK and cations.

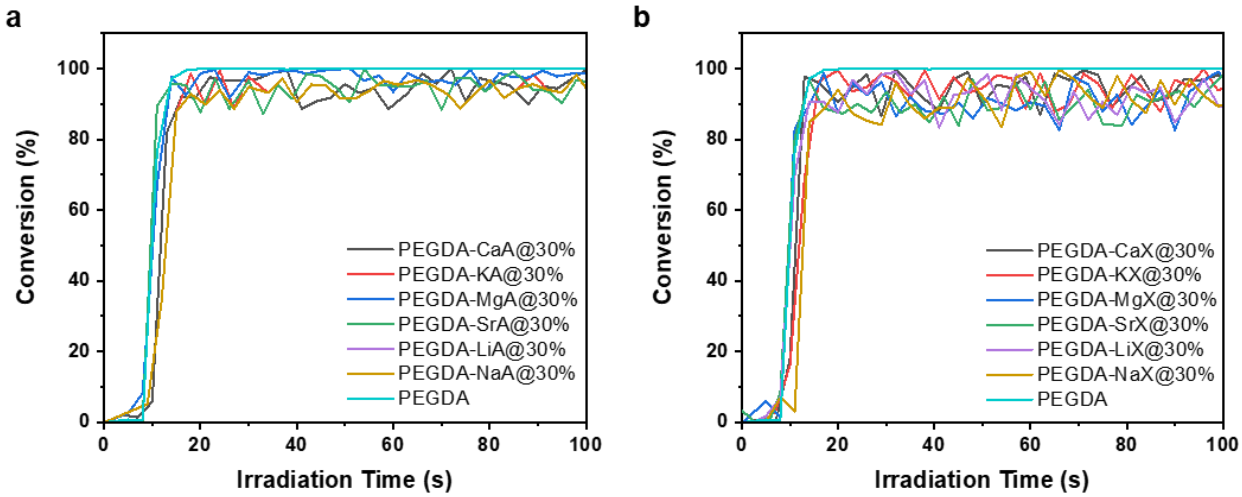

Figure 2. Polymerization profiles of filled resins (acrylate functions conversion vs irradiation time) initiated by BDMK upon exposure to LED@405 nm under air (thickness = 2 mm): (a) 30 wt% of exchanged LTA in PEGDA, and (b) 30 wt% of exchanged FAU in PEGDA. The irradiation starts at t = 10 s.

It can be seen from the SEM images (Figure 3) that the zeolite particles of LTA (NaA) and FAU (NaX) are homogenously dispersed in PEGDA polymer at the concentration of 30 wt%. No obvious zeolite aggregation or polymer shrinkage was observed in the composites, indicating a good compatibility between the polymer and zeolite. Thanks to the homogeneity of the filler distribution, colorimetric analyses can be further conducted on these polymer/zeolite composites.

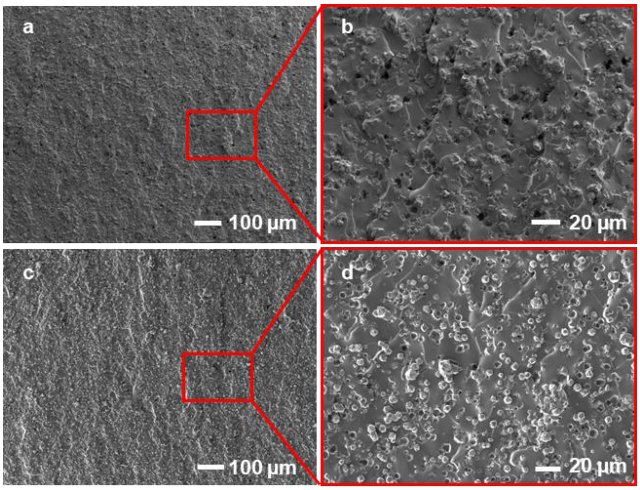

Figure 3. SEM images of the cross sections for polymer/zeolite composites containing 30 wt% zeolite: (a-b) PEGDA-NaA@30%, (c-d) PEGDA-NaX@30%.

The DOC, TP and other colorimetric parameters including a*, b* and L* for different polymer/zeolite composites are summarized in Table 3. The results indicate that the nature of cations in zeolite can affect the colorimetric properties of composites. In addition, LTA based composites exhibit greater light transmission (higher TP values) and higher DOC compared to composites with FAU. As the two zeolite types are characterized by non-identical crystal morphologies (FAU: twinned octahedra; LTA: well-shaped cubes), results could be explained by this difference of crystal shapes, which could affect zeolite refractive indices.

Table 3. DOC, TP and other colorimetric parameters (a^*, b^* and L^*)[1] of polymer/zeolite composites with exchanged zeolites at filler content of 30 wt%.

Composites	**DOC (mm)**	**TP**	***a****	***b****	***L****
PEGDA-NaA@30%	6.74 (0.05)	22.60 (0.46)	-0.77 (0.08)	15.50 (0.24)	16.43 (0.44)
PEGDA-LiA@30%	8.56 (0.17)	30.75 (0.60)	-0.11 (0.05)	21.04 (0.26)	22.42 (0.58)
PEGDA-KA@30%	7.81 (0.07)	28.30 (0.56)	0.39 (0.12)	19.67 (0.33)	20.34 (0.49)
PEGDA-SrA@30%	6.35 (0.07)	20.30 (0.34)	0.06 (0.09)	14.96 (0.18)	13.73 (0.31)
PEGDA-CaA@30%	8.12 (0.08)	27.27 (0.31)	-1.08 (0.06)	18.76 (0.12)	19.76 (0.33)
PEGDA-MgA@30%	6.20 (0.04)	25.37 (0.44)	1.90 (0.05)	18.85 (0.25)	16.88 (0.39)

PEGDA-NaX@30%	4.28 (0.03)	8.32 (0.09)	1.43 (0.11)	5.95 (0.29)	5.64 (0.24)
PEGDA-LiX@30%	4.26 (0.04)	8.51 (0.12)	1.53 (0.08)	6.12 (0.23)	5.70 (0.37)
PEGDA-KX@30%	5.32 (0.03)	9.23 (0.24)	2.25 (0.08)	6.90 (0.23)	5.70 (0.16)
PEGDA-SrX@30%	4.34 (0.01)	8.25 (0.12)	1.60 (0.10)	6.40 (0.14)	4.95 (0.29)
PEGDA-CaX@30%	5.31 (0.07)	8.92 (0.30)	2.66 (0.04)	6.48 (0.15)	5.52 (0.49)
PEGDA-MgX@30%	5.10 (0.02)	8.86 (0.13)	1.92 (0.06)	6.46 (0.10)	5.75 (0.23)

[1] a^*, b^*, L^* are calculated by $a^* = a^*_w - a^*_b$, $b^* = b^*_w - b^*_b$ and $L^* = L^*_w - L^*_b$ respectively.

As reported in the literature, the composite becomes more translucent when the mismatch of refractive indices between polymer and filler decreases.[32] Among the exchanged LTA, PEGDA-LiA@30% composite presents the highest DOC (8.56 mm) and TP (30.75), which are respectively 35% and 51% greater than those values of PEGDA-SrA@30%. However, the difference in TP between the composites with exchanged FAU is less pronounced. In general, as illustrated in Figure 4a and 4b, DOC becomes greater as TP increases. As the morphologies and sizes of zeolite particles remain unchanged before and after ion exchange (except for MgA), we can assume that the nature of cations has an impact on the optical properties (ca. colorimetric properties and refractive indices) of zeolites. The shift in optical property should be due mainly to different cations modifying the position and quantity of water molecules in micropores, which will further affect the light scattering in polymer/zeolite composites.[44] However, no clear correlation was observed between the water content of zeolite and the TP of polymer/zeolite composite in our study (Figure S7).

In addition, the colorimetric properties of the composites are also strongly affected by the filler content (Table S1). Particularly, b* and L* decrease with increasing filler content. The relatively high b* value is attributed to the yellowing effect of BDMK, which is most pronounced in the pure PEGDA polymer without zeolite filler. However, upon incorporating zeolites (white powders) into the composites, they become more opaque and exhibit a whitened appearance, resulting in a reduction in the yellowing (b*) and lightness (L*) parameters. Figure 4c and 4d demonstrate the TP decreases when filler content increases. Furthermore, the decreasing trend of TP slows down and approaches a specific value. As the filler content increases, the light that is reflected, refracted and absorbed by filler particles increases. As a

result, the intensity of penetrated light decreases and the opacity of composite increases (smaller TP). The colorimetric analysis is interesting as the optical properties can be adjusted with the compensating cations of the zeolites and the filler content. This can be a huge advantage for zeolite considered as fillers in the fields where optical or esthetic properties are crucial (e.g., holographic sensors and dental materials). For instance, polymers filled with low zeolite content were developed as dental materials for potential remineralizing or antibacterial effects.[45–47] Doping of photopolymers with nanosized zeolites alters the optical characteristics, which is of significant relevance to the study of holographic sensors.[48,49]

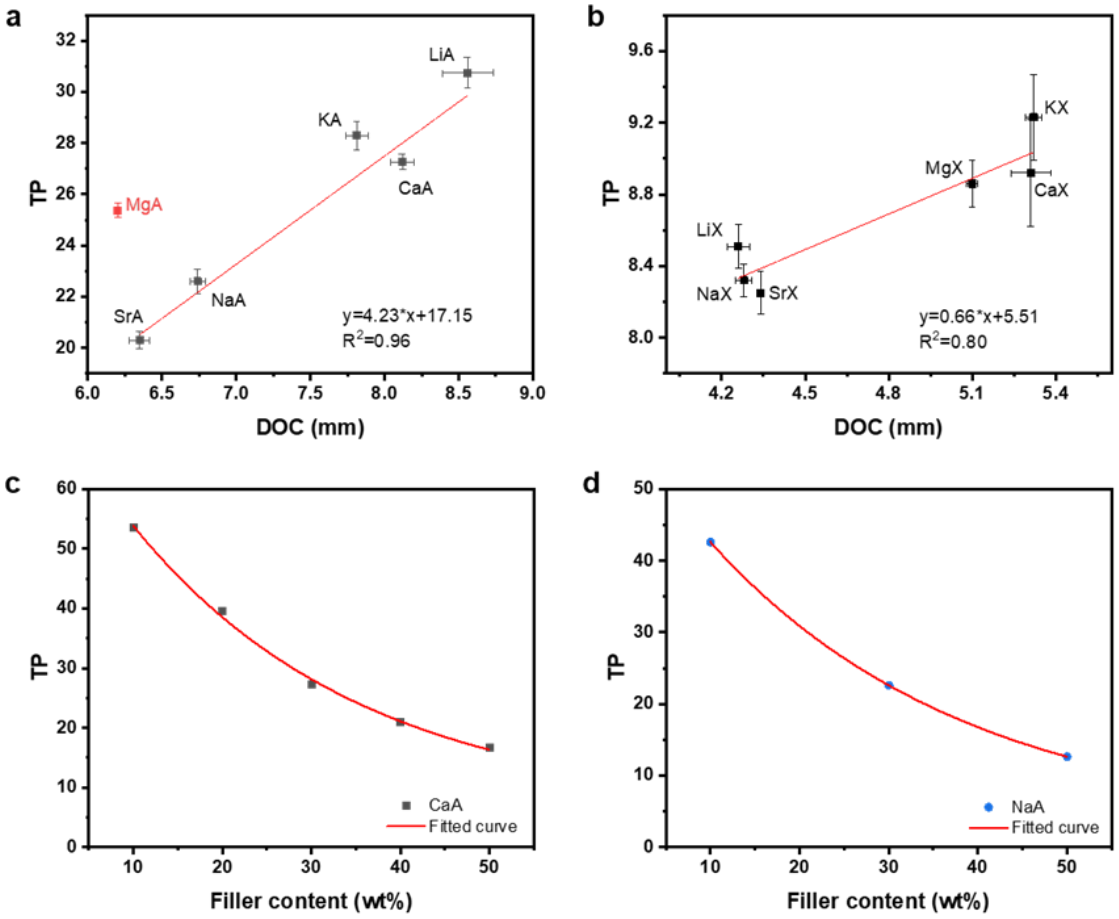

Figure 4. TP vs. DOC for polymer/zeolite composites: (a) exchanged LTA (MgA was not included for the fitting due to the morphological change), and (b) exchanged FAU. TP vs. zeolite contents at 10-50 wt%. (c) PEGDA-CaA, and (d) PEGDA-NaA.

Gas adsorption by calcined composites

N_2 adsorption-desorption

3D printed composites *via* layer-by-layer modeling were calcined at 650 °C for different durations. The nitrogen adsorption-desorption isotherms of the calcined composites are reported in Figure 5. For LTA based samples, comparable S_{BET} and V_{micro} are observed in the m-CaA-650°C-4h to its pristine powder form (Table 4). On the other hand, the m-SrA-650°C-4h shows a significant decrease of 51% in S_{BET} compared to its pristine powder and m-MgA-650°C-4h exhibits a higher S_{BET}, with an increase of 13% compared to the MgA powder. These variations in S_{BET} and V_{micro} can be related to the effect of compensation cations upon heating. The cations are partially or completely coordinated by water molecules. When heated, the compensation cation loses the bonded water molecules and are forced to move closer to the framework oxygens to form new bonds. This mechanism will eventually induce the change of pore aperture and, in some cases, even lead to phase collapse.[50]

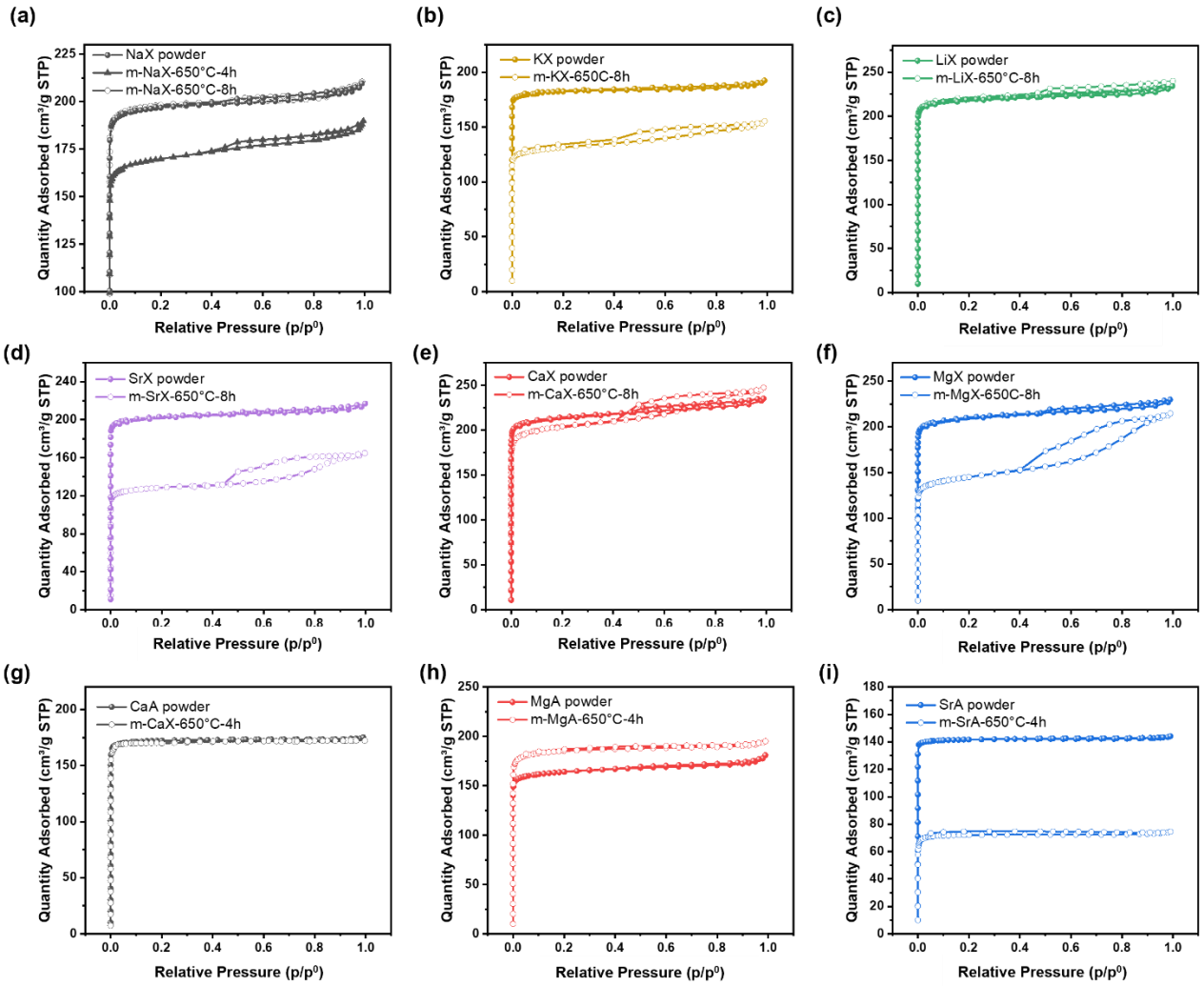

Figure 5. N_2 adsorption/desorption isotherms for ion-exchanged FAU or LTA composites after calcination at 650 °C for 4/8 hours.

For the Na-FAU based calcined composite, compared to the pristine powder, S_{BET} decreases by 10% after four hours of calcination (815 m^2 g^{-1} for NaX powder and 731 m^2 g^{-1} for m-NaX-650°C-4h), but returns to the same value of its powder form after eight hours of calcination. This may be a result of the larger pore aperture of FAU (0.74 nm) compared to LTA (0.3-0.5 nm), which traps more easily the residual organic compounds from polymer/photoinitiator decomposition that take longer to evaporate. Therefore, the calcination duration at 650 °C for composites containing LTA and FAU zeolite was set at 4 hours and 8 hours, respectively. Among the calcined composites based on ion-exchanged FAU, only m-

NaX-650°C-8h and m-LiX-650°C-8h retained their original porosity compared to their pristine powders. Ca^{2+}, K^{+}, Sr^{2+}, and Mg^{2+} exchanged FAU has a decrease in porosity after calcination. The decreases are respectively 6%, 30%, 38% and 33% for CaX, KX, SrX and MgX respectively. Additionally, the formation of mesopores was observed in the m-CaX-650°C-8h, m-MgX-650°C-8h, and m-SrX-650°C-8h samples.

Table 4. Textural properties of the calcined composites in comparison with their pristine powder.

	S_{BET} (m^2/g)	S_{micro} (m^2/g)	S_{ext} (m^2/g)	V_{micro} (cm^3/g)
CaA powder	720	720	0	0.26
m-CaA-650°C-4h	718	718	0	0.26
SrA powder	615	613	2	0.22
m-SrA-650°C-4h	299	298	1	0.11
MgA powder	672	660	12	0.25
m-MgA-650°C-4h	758	750	8	0.29
NaX powder	815	803	12	0.30
m-NaX-650°C-4h	731	696	35	0.26
m-NaX-650°C-8h	815	808	7	0.30
LiX powder	902	891	11	0.34
m-LiX-650°C-8h	901	883	18	0.33
KX powder	760	752	8	0.28
m-KX-650°C-8h	533	495	38	0.19
CaX powder	869	843	26	0.32
m-CaX-650°C-8h	815	744	71	0.28
SrX powder	836	826	10	0.31
m-SrX-650°C-8h	520	444	76	0.15
MgX powder	857	838	19	0.32
m-MgX-650°C-8h	571	486	85	0.19

H_2O vapor adsorption

As LTA are well-known as desiccants, water adsorption capacity of the calcined composites has been determined. Based on the results of N_2 adsorption-desorption, m-MgA-650°C exhibits the highest S_{BET} and V_{micro}. Therefore, this sample was selected for the water adsorption in comparation with the NaA

powder before ion-exchange and the commercial NaA beads. Figure 6 displays the water adsorption isotherms, and the water adsorption capacities were determined at $p/p^0 = 0.2$, representing the adsorption within the microporosity of the samples. Clearly, the calcined MgA composite exhibits the highest water adsorption capacity (ca. 13.7 mmol/g), exceeding the NaA commercial beads (ca. 11.0 mmol/g) by 24% and the NaA powder (ca. 12.7 mmol/g) by 8%. This value is agreement with the capacity reported by Tahraoui et al., who measured a capacity of 14.7 mmol/g for Mg-exchanged LTA (exchange rate = 68%).[51] Moreover, at relative pressure above 0.05 (corresponding to a relative humidity of 5%) the calcined MgA composite is more efficient than commercial beads, and above 0.12 (corresponding to a relative humidity of 12%) it becomes more effective than NaA powder.

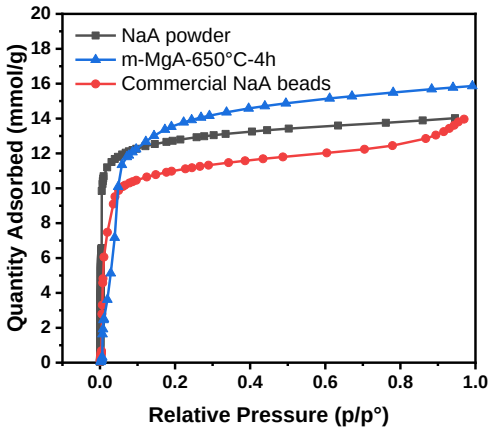

Figure 6. H_2O vapor adsorption for NaA powder, commercial beads and calcined MgA composites.

1,2-diclorobenzene adsorption

The porosity of FAU zeolite allows for effective adsorption of polychlorobenzenes, which are important precursors in the formation of dioxin/furan compounds and are commonly used as models in the investigation of dioxin adsorption.[52] In this study, 1,2-dichlorobenzene was selected as a representative polychlorobenzene and adsorbed onto FAU zeolite monoliths. The adsorption kinetics were investigated and reported in Figure 7. A slow adsorption process was observed and saturation is not achieved after 40 h. This behavior can be explained by the low vapor pressure of 1,2-dichlorobenzene at 25 °C (1.36 mm Hg).

It appears that the calcined CaX composite (m-CaX-650°C-8h) exhibits highest adsorption rate for the first 27 hours, after which the commercial NaX beads outperform it. At adsorption time t = 38 h, the adsorption capacity of commercial beads is 310 mg/g. For the calcined CaX, NaX, and SrX monoliths, the adsorption capacity decreases by 9%, 12%, and 34%, respectively. The adsorption capacities for calcined CaX and NaX composites are comparable to, or even higher than those reported by Rioland et al., for the FAU beads fabricated with CMC or Na_2SiO_3 as binders (the highest adsorption capacity observed in their study was 273 mg/g at saturation).[53] By extrapolation for longer time, the lower adsorption capacity for CaX and SrX can be attributed to the decreased V_{micro} compared to NaX (Table 4). As the same S_{BET} and porous volume were obtained for m-NaX-650°C-8h as for the NaX powder, the decrease of 1,2-dichlorobenzene adsorption rate at high adsorption time compared to the commercial beads could only be explained by the longer diffusion length in printed monolith (diameter: 3-4 mm for printed monoliths compared to 2 mm for commercial beads).

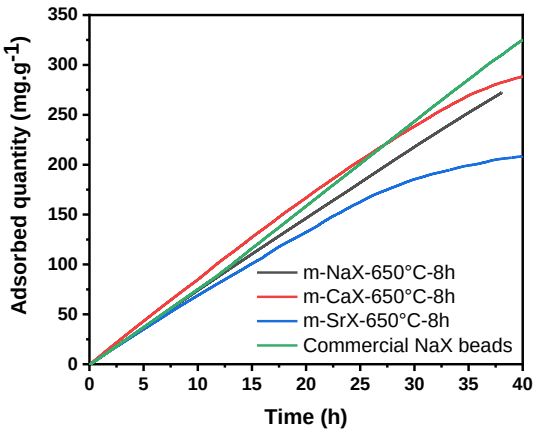

Figure 7. Adsorption of 1,2-dichlorobenzene (25 °C, p/p° = 0.5) on commercial beads and calcined FAU composites**.**

CO_2 adsorption

CO_2 adsorption isotherms recorded at 20°C of ion-exchanged FAU powder and their calcined monoliths, as well as the NaX commercial beads are shown in Figure 8. The CO_2 adsorption capacity of

LiX, NaX, KX, MgX, CaX and SrX are 6.68, 6.41, 5.50, 4.67, 5.86 and 5.95 mmol/g, respectively. It is evident that the NaX and LiX monoliths prepared by 3D printing display comparable adsorption capacities to their powders and the commercial beads (6.05 mmol/g). In particular, m-NaX-650°C-8h shows a CO_2 uptake of 5.85 mmol/g which is 91% of that of NaX in the powder form, while m-LiX-650°C-8h exhibits 90% of the capacity of the LiX powder. However, it should be noted that the adsorption capacity of calcined SrX, KX, CaX, and MgX composites is significantly lower compared to their pristine powders, representing only 54%, 68%, 66%, and 77% of their original capacity, respectively. This decrease in adsorption capacity can be attributed to the reduction in specific surface area observed after the shaping followed by the calcination process, as depicted in Figure 7 and outlined in Table 4.

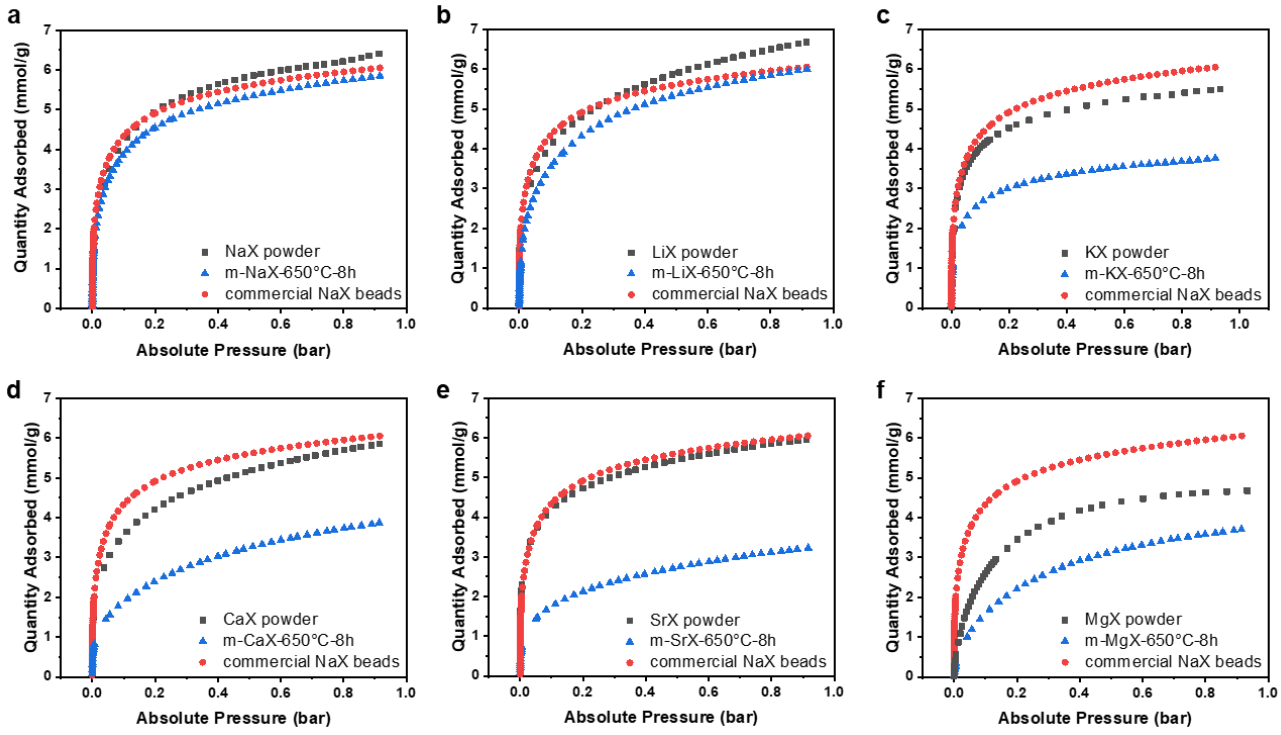

Figure 8. CO_2 adsorption isotherms at 20°C for (a) NaX powder and its calcined monolith, (b) SrX powder and its calcined monolith (c) LiX powder and its calcined monolith (d) CaX powder and its calcined monolith (e) SrX powder and its calcined monolith and (f) MgX powder and its calcined monolith. The commercial NaX beads were inserted as a reference.

Conclusions

In this work, we have successfully prepared structured polymer/zeolite-based composites and their calcined zeolitic monoliths *via* 3D printing at 405 nm LED irradiations under mild conditions. To the best of our knowledge, this is the first reported investigation into the impact of zeolite compensation cations on photopolymerization and colorimetric characteristics. The results indicate that the compensation cations have no effect on the polymerization kinetics, but do have an effect on the optical properties of composites. For composites filled with LTA zeolites, the translucency parameter (TP) which characterizes the opacity of composites, decreases in the following order: $Li^+ > K^+ > Ca^{2+} > Na^+ > Sr^{2+} > Mg^{2+}$ (surface roughness). For FAU, the order is $K^+ > Ca^{2+} > Mg^{2+} > Li^+ > Na^+ > Sr^{2+}$. We assume that the nature of cations influencing their location in the zeolite structure and the water amount in the zeolites, which affects the zeolites' refractive indices and light scattering in the composites. The possibility to tailor the colorimetric properties by modifying the compensation cations or zeolite content, is of great interests in the fields of holographic sensors and medicinal materials.

However, it's worth noting that cations can have a significant impact on the thermal stability of zeolites, potentially causing challenges during the calcination process, which aims to eliminate the polymer and create porosity. The S_{BET} and V_{micro} of the exchanged zeolites were significantly affected by the shaping process followed by calcination. The MgA exchanged zeolites, in particular, showed high hydrophilicity and a significant increase in specific surface area after calcination, surpassing that of commercial beads in terms of water adsorption capacity. On the other hand, the adsorption capacity of CO_2 on calcined SrX, MgX, CaX, and KX monoliths decreased compared to their pristine powders. In terms of adsorption of 1,2-dichlorobenzene adsorption, calcined CaX and NaX monoliths produced positive results that were comparable to those of commercial beads. Furthermore, the calcined NaX and LiX monoliths maintained a similar specific surface area as their pristine powder counterparts, which

ensured their effectiveness in gas adsorption performance. These characteristics make them suitable candidates for 3D printing to create intricate structures.

This work is intended to expand our understanding of the polymer/zeolite-based composite and to contribute to the fields of functional composites, adsorption materials, 3D printing and zeolite shaping.

Experimental section

Materials

The oligomer poly(ethylene glycol) diacrylate (PEGDA, $M_w \approx 600$) was purchased from Sartomer (SR610). The photoinitiator 2-benzyl-2-(dimethylamino)-4'-morpholinobutyrophenone (BDMK), LTA-4A (NaA) powder and LTA-4A beads (8-12 mesh), $Mg(NO_3)_2.6H_2O$ (99%) were obtained from Sigma-Aldrich. Binder free FAU 13X beads (10-16 mesh) were supplied by Chemiewerk Bad Köstritz GmbH. FAU 13X powder (NaX), $Ca(NO_3)_2.4H_2O$ (> 99%), $Sr(NO_3)_2$ (> 99%), KNO_3 (≥ 99%) and $LiNO_3$ (≥ 99%) were purchased from Alfa Aesar, Acros Organics, Strem Chemicals, Carlo Erba and Fluka respectively. The dispersant BYK-180 was obtained from BYK Additives & Instruments.

The molecular structures of PEGDA and BDMK are shown in Figure 9.

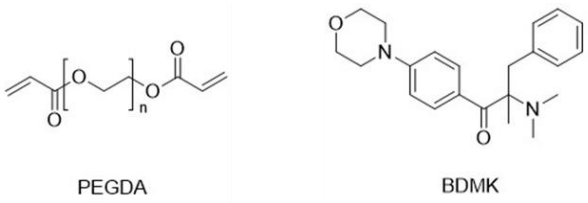

Figure 9. Chemical structure of monomer (PEGDA) and photoinitiator (BDMK) in this work.

Synthesis of ion-exchanged zeolites

Ion-exchanged zeolites were carried out from NaA and NaX zeolites. Parent zeolite was soaked into 0.1 M aqueous solutions of KNO_3, $LiNO_3$, $Ca(NO_3)_2$, $Sr(NO_3)_2$ or $Mg(NO_3)_2$ with a liquid/solid ratio of 50:1 (mL/g). The exchange procedure was repeated three times at 60 °C under magnetic stirring and each exchange lasted for 2 h. Following the exchange, the solids were washed with deionized water and dried

at 100 °C in an oven overnight. The exchanged zeolites were named *Me*A for LTA type and *Me*X for FAU type, where *Me* = K^+, Li^+, Ca^{2+}, Sr^{2+} or Mg^{2+}.

Preparation of polymer/zeolite composites

Photoinitiator BDMK was dissolved in PEGDA at a weight ratio of 1/100. Then, zeolite was added to the PEGDA/BDMK mixture at a weight ratio of 30/70 and homogenized with SpeedMixer (DAC 150.1 FVZ-K) at 2000 rmp for 2 minutes. For depth of cure (DOC) measurement, the mixture was transferred into an opaque mold made of rubber (unsealed from the top) before irradiation with a LED lamp for 30 s (LED@405 nm; 1W/cm^2). As illustrated in Figure 10, the cured part on the top was washed with acetone to remove the residual resin, and then its thickness was measured with an Absolute LCD Digimatic Indicator (Mitutoyo). As-prepared polymer/zeolite composites were named PEGDA-*Me*A (or *Me*X)@*n*%, where *n* is the weight percentage of zeolite in composites.

For the colorimetric analysis, composites were prepared in a cylindrical mold of Teflon (diameter = 12 mm and thickness = 2 mm) between two glass slides to ensure flat surfaces.

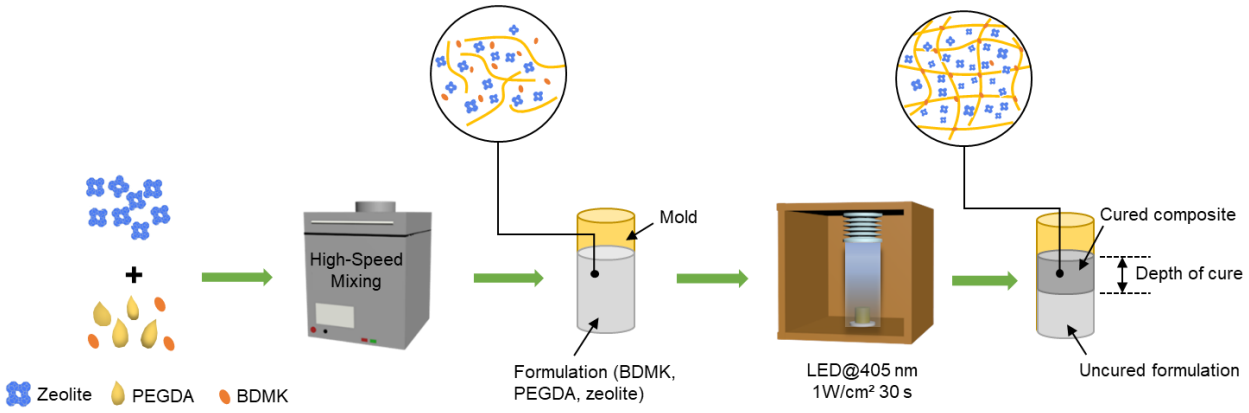

Figure 10. Preparation of polymer/zeolite composite *via* photopolymerization and DOC determination.

3D structure development

Some three-dimensional structures were successfully produced using a home-made 3D printer (Figure 11a). The printer consists of an air bump and a pressure controller to regulate the deposition pressure, an adjustable platform with adjustable X, Y, and Z axes for printing direction control, and an

injection syringe for formulation deposition. The 3D printing process consists of two main steps, i) layer deposition and ii) photopolymerization. The ink formulation is extruded through a nozzle (diameter = 1.19 mm) and deposited on the adjustable platform with a nozzle movement speed of 1.5 mm/s. After deposition of one layer of formulation, the layer was cured by a LED lamp (405 nm). The subsequent layer was printed directly on top of the preceding layer and the photopolymerization was performed again until the 3D structure was obtained. We had to balance achieving high solid loading and maintaining the ink formulation's fluidity. Here, the zeolite content was set at 57 wt% and BYK-180 was added (1 wt% of the formulation) to decrease the viscosity for a shear thinning property.[54]

The printed zeolite-embedded composites with various geometries are demonstrated in Figure 11b and 11c. After calcination at 650 °C during 4 or 8 hours under air (calcination profile in Figure S1), PEGDA polymer was completely removed and pure zeolitic monoliths were obtained, retaining the shape and size of polymer/zeolite composites. Calcined composites (monoliths) were named m-*Me*A (or *Me*X)-650 °C-*n*h, where *n* is the calcination time (hours) at 650 °C.

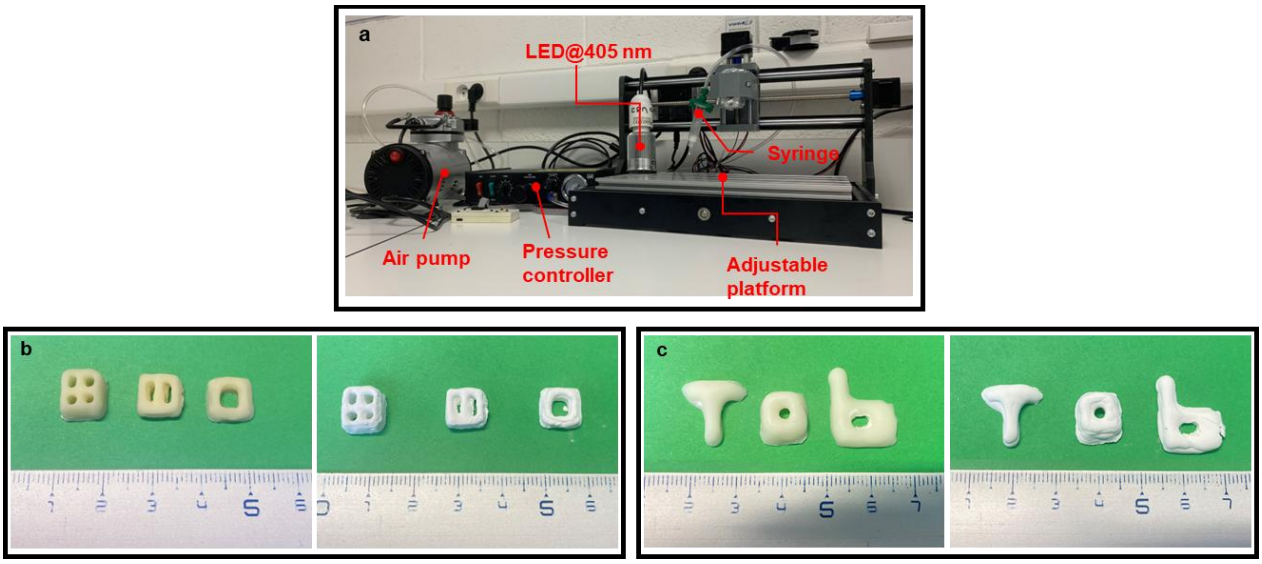

Figure 11. Scheme of (a) the home-made robocasting 3D-printer used in this study, (b-c) the printed zeolite-embedded composites (PEGDA-NaA@55%) with various geometries (left) before calcination and (right) after calcination at 650 °C.

Characterization techniques

The crystalline structure of exchanged zeolites was identified by X-ray diffraction (XRD) measurements using a PANalytical MPD X'Pert Pro diffractometer operating with Cu Kα radiation (Kα = 0.15418 nm) equipped with an PIXcel real-time multiple strip detector (active length = 3.347 ° (2θ)). The powder patterns were collected at 295 K in the range 3 ° < 2θ < 70 ° with a step of 0.013 ° (2θ) and a time/step equal to 220 s. Elemental analyses were performed by X-Ray Fluorescence spectrometry (XRF) with a PANalytical Zetium (4 kW) spectrometer. Samples were mixed with boric acid and pressed into pellets of 13 mm diameter with 5 tons of pressure before the analysis.

The crystal sizes and morphologies of zeolites were investigated by scanning electron microscopy (SEM) using a JEOL JSM-7900 F model. The EDX (Energy Dispersive X-ray) analyses and element mappings were performed using a JOEL Centurio detector. To measure the water content in zeolites, thermogravimetric analyses (TGA) using a METTLER-TOLEDO TGA/DSC 3+ thermoanalyzer were recorded under air with a heating rate of 5 °/min until 800 °C. All zeolites were equilibrated for 2 days in in a dessicator over saturated NaCl solution (75% relative humidity) before TGA analyses.

Nitrogen (N_2) adsorption-desorption isotherms were performed at -196 °C with a Micromeritics ASAP 2420 Instrument. Prior to N_2 sorption measurement, samples were outgassed to a residual pressure of less than 0.8 Pa at 300 °C for 15 h in order to remove adsorbed water. The surface area (S_{BET}) was determined using the BET method (relative pressure $p/p°<0.05$). The *t*-plot method using the Harkins-Jura thickness equation was used to determine the microporous volume (V_{micro}).

The measurement of the DOC was realized with an Absolute LCD Digimatic Indicator (Mitutoyo) after exposing to a LED lamp for 30 s. The photopolymerization process was followed through the C=C double bond conversion in PEGDA for thick samples (2 mm) with real-time Fourier transformed infrared spectrometer (RT-FTIR, JASCO FTIR 4600) equipped with a LED@405 nm (intensity = 110 mW/cm²). Because zeolites have an adsorption at 1600 cm^{-1} (water bending), which is also associated to C=C

stretching for acrylate, the conversion during polymerization is therefore calculated based on the intensity decline of the combination band at about 6100 cm^{-1} *vs*. irradiation time, as set out in equation (2).

$$FC = \frac{A_0 - A_t}{A_0} \times 100 \qquad \text{Equation (2)}$$

Where FC is the final conversion (%), A_0 is the initial peak area at t = 0 s and A_t is the peak area at t s.

For the colorimetric analysis of the composites, C.I.E. (International Commission on Illumination) colorimetric coordinates such as L^* (lightness axis), a^* (red-green axis), b^* (yellow-blue axis) of cylindrical specimens (diameter r = 12 mm, thickness = 2 mm) were measured for each composites using a calibrated reflection spectrophotometer (Color-guide 45°/0° device, BYK Gardner company), against either a white (L^*_w = 94.74, a^*_w = -1.00, b^*_w = 0.10) or a black (L^*_b = 7.26, a^*_b = -0.99, b^*_b = -1.66) or a black background (C.I.E. D65 illuminant and the C.I.E. 45°/0° geometry). Translucency Parameter (TP) was calculated for each composite by Equation (3):

$$TP = [(L*_w - L*_b)^2 + (a*_w - a*_b)^2 + (b*_w - b*_b)^2]^{1/2} \qquad \text{Equation (3)}$$

where TP ranges between 0 (opaque material) to 100 (translucent material).[55]

Adsorption experiments

The 3D printed structures were calcined under 650 °C during 4/8 hours (Figure S1) before adsorption of gas molecules of interest.

The adsorption measurements of 1,2-dichlorobenzene have been conducted in gas phase using a Setaram®TGA "SETSYS Evolution" thermobalance under dynamic conditions. All samples were activated at 400°C during 2 hours under nitrogen. The sorption of organic vapor was then performed at 25°C with a relative pressure of p/p° = 0.5 (p is the vapor pressure and p° is the saturation vapor pressure of 1,2-dichlorobenzene at 25 °C i.e., p° = 1.36 mmHg). The relative pressure p/p° = 0.5 was obtained by setting the gas flow of auxiliary gas (N_2 + 1,2-dichlorobenzene) and carrier gas (N_2) to 30 mL min^{-1} at the inlet of the oven. The weight variations of the zeolitic samples were recorded during the time of

adsorbent-adsorbate contact.

The CO_2 adsorption capacity of the composites after calcination has been achieved at 20 °C with a Micromeritics ASAP 2420 Instrument from 0-0.9 bar. Prior to the measurement, samples were outgassed to a residual pressure of less than 0.8 Pa at 300 °C for 15 h.

Water vapor adsorption–desorption isotherms were performed at 25 °C using a Micromeritics 3Flex Instrument. The samples (50–100 mg) were outgassed under vacuum at 300 °C for 24 h to remove physisorbed water. Prior to water adsorption experiments, water was flash frozen under liquid nitrogen and then evacuated under dynamic vacuum at least five times to remove any gases in the water reservoir. The water adsorption capacity was determined from water adsorption isotherms.

Acknowledgements

We would like to thank Ludovic Josien and Laure Michelin for their assistance with the SEM and XRD/XRF tests, respectively. In addition, we would like to thank Adrien Beda and Cyril Vaulot for their help with the adsorption experiments.

Reference

[1] L. Zhang, Y. Peng, J. Zhang, L. Q. Chen, X. Meng, F.-S. Xiao, *Chinese J. Catal.* **2016**, *37*, 800-809.

[2] G. Singh, J. M. Lee, A. S. Karakoti, R. Bahadur, J. Yi, D. Zhao, K. Al-Bahily, A. Vinu, *Chem. Soc. Rev.* **2020**, *49*, 4360-4404.

[3] S. Kesraoui-Ouki, C. R. Cheeseman, R. R. Perry, *J. Chem. Technol. Biotechnol.* **1994**, *59*, 121-126.

[4] D. M. Ruthven, *Principles of adsorption and adsorption processes*, John Wiley & Sons, **1984**, p. 13.

[5] E. Lalik, R. Mirek, J. Rakoczy, A. Groszek, *Catal. Today* **2006**, *114*, 242-247.

[6] H. Sun, D. Wu, X. Guo, B. Shen, J. Liu, A. Navrotsky, *J. Phys. Chem. C* **2014**, *118*, 25590-25596.

[7] R. Navarrete-Casas, A. Navarrete-Guijosa, C. Valenzuela-Calahorro, J. D. López-González, A. García-Rodríguez, *J. Colloid Interface Sci.* **2007,** *306*, 345-353.

[8] H. S. Kim, S. Y. Choi, W. T. Lim, *J. Porous Mater.* **2013**, 20, 1449-1456.

[9] A. Top, S. Ülkü, *Appl. Clay Sci.* **2004**, *27*, 13-19.

[10] H. Wu, F. Salles, J. Zajac, *Molecules* **2019**, *24*, 945.

[11] R. T. Yang, *Adsorbents: fundamentals and applications*, John Wiley & Sons, **2003**, p. 160.

[12] T. Frising, P. Leflaive, *Microporous Mesoporous Mater.* **2008**, *114*, 27-63.

[13] R. Bingre, B. Louis, P. Nguyen, *Catalysts* **2018**, *8*, 163.

[14] K. Kennes, A. V. Kubarev, C. Demaret, L. Treps, O. Delpoux, M. Rivallan, E. Guillon, A. Methivier, T. De Bruin, A. Gomez, B. Harbuzaru, M. B. J. Roeffaers, C. Chizallet, *ACS Catal.* **2022**, *12*, 6794-6808.

[15] J. Lefevere, L. Protasova, S. Mullens, V. Meynen, *Mater. Des.* **2017**, *134*, 331-341.

[16] S. Lawson, X. Li, H. V. Thakkar, A. A. Rownaghi, F. Rezaei, *Chem. Rev.* **2021**, *121*, 6246-6291.

[17] M. J. Regufe, A. R. Ferreira, J. M. Loureiro, A. E. Rodrigues, A. C. F. Ribeiro, *Microporous Mesoporous Mater.* **2019**, *278*, 403-413.

[18] H. V. Thakkar, S. Eastman, A. N. Hajari, A. A. Rownaghi, J. C. Knox, F. Rezaei, *ACS Appl. Mater. Interfaces* **2016**, *8*, 27753-27761.

[19] H. V. Thakkar, S. Lawson, A. A. Rownaghi, F. Rezaei, *Chem. Eng. J.* **2018**, *348*, 109-116.

[20] S. Couck, J. Cousin-Saint-Remi, S. Van Der Perre, G. Baron, C. Minas, P. Ruch, J. Denayer, *Microporous Mesoporous Mater.* **2018**, *255*, 185-191.

[21] S. Couck, J. Lefevere, S. Mullens, L. Protasova, V. Meynen, G. Desmet, G. Baron, J. Denayer, *Chem. Eng. J.* **2017**, *308*, 719-726.

[22] S. Wang, B. Pu, M. Sun, W. Liu, D. Li, W. Wenzheng, W. Yan, K.-Y. A. Lin, J. Yu, *Adv. Sci.* **2019**, *6*, 1901317.

[23] X. Li, W. Li, F. Rezaei, A. A. Rownaghi, *Chem. Eng. J.* **2018**, *333*, 545-553.

[24] L. Sa, L. Kaiwu, C. Shenggui, Y. Junzhong, J. Yongguang, W. Lin, R. Li, *J. Mater. Sci.* **2018**, *54*, 3309-3318.

[25] M. Sangermano, G. Malucelli, E. Amerio, A. Priola, E. Billi, G. Rizza, *Prog. Org. Coat.* **2005**, *54*, 134-138.

[26] Y. Zhang, K. Hasegawa, K. Sota, K. Takagi, A. Takahara, *Polymer* **2020**, *209*, 123036.

[27] M. Pagáč, J. Hajnys, Q.-P. Ma, L. Jancar, J. Jansa, P. Stefek, J. Mesicek, *Polymers* **2021**, *13*, 598.

[28] Y. Zhang, Y. Gao, L. Josien, H. Nouali, C. Vaulot, A. Simon-Masseron, J. Lalevée, *Adv. Mater. Technol.* **2021**, *7*, 2100869.

[29] Y. Zhang, Y. Gao, L. Michelin, L. Josien, L. Vidal, G. Schrodj, A. Simon-Masseron, J. Lalevée, *Eur. Polym. J.* **2022**, *179*, 111552.

[30] Y. Gao, Y. Zhang, J. Lalevée, A. Simon-Masseron, *ACS Appl. Nano Mater.* **2023**, *6*, 10156–10167.

[31] Y. Gao, Y. Zhang, L. Michelin, J. Lalevée, A. Simon-Masseron, *Mater. Chem. Phys.* **2023**, *293*, 126853.

[32] A. C. Shortall, W. M. Palin, P. Burtscher, *J. Dent. Res.* **2008**, *87*, 84-88.

[33] H. Schulz, P. Burtscher, L. Mädler, *Composites Part A* **2007**, *38*, 2451-2459.

[34] M. Kawaguchi, T. Fukushima, K. Miyazaki, *J. Dent. Res.* **1994**, *73*, 516-521.

[35] H. S. Sherry, *J. Phys. Chem.* **1966**, *70*, 1158-1168.

[36] R. A. Rakoczy, Y. Traa, *Microporous Mesoporous Mater.* **2003**, *60*, 69-78.

[37] H. Lührs, J. Derr, R. Fischer, *Microporous Mesoporous Mater.* **2012**, *151*, 457-465.

[38] L. L. Price, K.-M. Leung, A. Sartbaeva, *Magnetochemistry* **2017**, *3*, 42.

[39] Database of Zeolite structures, http://www.iza-structure.org/databases/

[40] M. Thommes, K. Kaneko, A. V. Neimark, J. P. Olivier, F. Rodríguez-Reinoso, J. Rouquerol, K. S. W. Sing, *Pure Appl. Chem.* **2015**, *87*, 1051-1069.

[41] D. W. Breck, W. G. Eversole, R. M. Milton, T. B. Reed, T. L. Thomas, *J. Am. Chem. Soc.* **1956**, *78*, 5963-5972.

[42] R. Fischer, M. Burianek, R. V. Shannon, *Eur. J. Mineral.* **2020**, *32*, 27-40.

[43] J. A. Palmer, M. E. Gunter, *Am. Mineral.* **2000**, *85*, 225-230.

[44] R. M. Barrer, J. Klinowski, *J. Chem. Soc.* **1972**, *68*, 1956-1963.

[45] Z. Buchwald, M. Sandomierski, A. Voelkel, *ACS Biomater. Sci. Eng.* **2020**, *6*, 3843-3854.

[46] Z. Okulus, M. Sandomierski, M. Zielińska, T. Buchwald, A. Voelkel, *Spectrochim. Acta* **2019**, *210*, 126-135.

[47] K. Kawahara, K. Tsuruda, M. Morishita, M. Uchida, *Dent. Mater.* **2000**, *16*, 452-455.

[48] T. Babeva, R. Todorov, S. Mintova, T. Yovcheva, I. Naydenova, V. Toal, *J. Opt.* **2009**, *11*, 024015.

[49] D. Cody, E. Mihaylova, L. a. J. O'Neill, T. Babeva, H. Awala, R. Retoux, S. Mintova, I. Naydenova, *Opt. Mater.* **2014**, *37*, 181-187.

[50] G. Cruciani, *J. Phys. Chem. Solids* **2006**, *67*, 1973-1994.

[51] Z. Tahraoui, H. Nouali, C. Marichal, P. Forler, J. Klein, T. J. Daou, T. J., *Molecules* **2020**, *25*, 944.

[52] K. Everaert, J. Baeyens, *J. Hazard. Mater.* **2004**, *109*, 113-139.

[53] G. Rioland, L. Bullot, T. J. Daou, A. Simon-Masseron, G. Chaplais, D. Faye, E. Fiani, J. Patarin, *RSC Adv.* **2016**, *6*, 2470-2478.

[54] L. J. Tan, W. Zhu, K. Zhou, *Adv. Funct. Mater.* **2020**, *30*, 2003062.

[55] M. Oivanen, F. Keulemans, S. Garoushi, P. K. Vallittu, L. V. J. Lassila, *Biomater. Invest. Dent.* **2021**, *8*, 48-53.

Table of Contents

Graphical abstract: The composition of zeolite influences the photopolymerization process of zeolite/polymer-based composites. The nature of compensation cations was examined to determine their effect on the opacity of the cured composite (*via* colorimetric analyses) and on the gas adsorption properties (for water, carbon dioxide and 1,2-dichlorobenzene) on calcined composites.